ARTICLE

Preparation of Iron and Gold Silicide Nanodomains on Silicon (111) by the Reaction of Gold, Iron–Gold Core–Shell, and Alloy Nanoparticles with Triethylsilane

Naween Dahal,[†] Joshua T. Wright,[‡] Trevor M. Willey,[§] Robert W. Meulenberg,[‡,||] and Viktor Chikan*[,†]

Department of Chemistry, Kansas State University, Manhattan, Kansas 66506-0401, Department of Physics and Astronomy and Laboratory for Surface Science and Technology, University of Maine, Orono, Maine 04469-5708, and Physical Sciences Directorate, Lawrence Livermore National Laboratory, Livermore, California 94550

ABSTRACT This study describes a strategy to use composite colloidal nanoparticles and triethylsilane as precursors to synthesize nanometer size structures on single-crystal silicon substrate. The concept is demonstrated by depositing gold, iron–gold alloy, and iron–gold core–shell nanoparticles on silicon (111). Upon heating, the nanoparticles form new crystalline phases on the Si (111) surface. Atomic force microscope (AFM) data show the collapse of the iron gold core–shell and alloy nanoparticles at temperatures 100–200 °C higher than gold nanoparticles, indicating the efficient tethering of iron containing nanoparticles on silicon (111). Both structural analysis and X-ray spectroscopy show that the iron–gold alloy and iron–gold core–shell nanoparticles successfully form the semiconducting β-$FeSi_2$ phase at relatively low temperature. The stabilities of the silicide are assessed at elevated temperatures. Silicon successfully nucleates on the created nanostructures, which suggests strong catalytic activity towards producing further nanostructures on the surface.

KEYWORDS: alloy • core–shell • nanoparticles • lattice • substrate • silicide

INTRODUCTION

Heterogeneous catalytic reactions are widespread and are commonly performed with the reactant(s) and product(s) in the liquid or gas phase and the catalyst in the solid phase, with the reaction occuring at the interface between the phases. The surface properties of a heterogeneously supported catalyst are significant factors in the effective use of that catalyst (1). The composite nanoparticles of iron and gold can also act as heterogeneous catalyst. Specifically, heating gold, iron–gold alloy, and iron–gold core–shell nanoparticles deposited on Si (111) can provide the accessible reaction sites through their interfaces. The reactions in the interfaces cause the reactant chemisorption and product desorption. This growth method allows the production of a large variety of novel nanostructures (2–7). Most heterogeneous catalysts are composed of a selected combination of active materials, promoter, and support. The implementation of combinatorial techniques to heterogeneous catalysis is a significantly more challenging problem than in other application areas of materials sciences (1). Additional challenges arise from the complex and dynamic nature of catalyst. If new sets of catalysts are used, the range of materials produced with the new catalysts can be significantly extended despite being complex and dynamic. In this manuscript, a novel idea is explored: oxidation-sensitive catalysts that can be prepared in a form that one can be used under atmospheric conditions, and still exhibit catalytic activity towards producing composite semiconductor nanostructures at elevated temperatures.

As a specific example, composite iron–gold alloy, core–shell, and gold nanoparticles are heated on Si (111) substrate in absence and presence of silicon precursor (triethylsilane). This method allows for the production of silicides of both iron and gold on the silicon substrate. Iron shows catalytic activity in producing gold silicide (Au_5Si_2) and gold shows the catalytic activity in producing iron silicide (β-$FeSi_2$) on the silicon substrate. However, colloidal iron nanoparticles are prone to oxidation, which seems to exclude the possibility to introduce iron nanoparticles from colloidal synthesis. Iron is the fourth most abundant element in the earth's crust, which would make iron a desirable material to address problem such as solar energy conversion (8–12) on a large scale. Effective bandgap calculations and experiments show that a decrease in the size of the β-$FeSi_2$ results in a direct bandgap (0.85 eV), leading to more efficient capture of photons and allowing some bandgap tunability upon quantum confinement (13, 14). The theoretical solar energy conversion efficiency of β-$FeSi_2$ is 16–23% (15). The beta iron silicide is non-toxic, ecologi-

* Author to whom all correspondence should be addressed.
Received for review March 30, 2010 and accepted June 28, 2010
[†] Kansas State University.
[‡] Department of Physics and Astronomy, University of Maine.
[§] Lawrence Livermore National Laboratory.
[||] Laboratory for Surface Science and Technology, University of Maine.
DOI: 10.1021/am100282q

Published on Web 07/15/2010

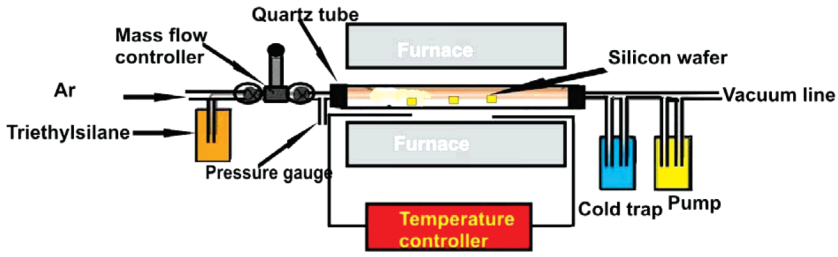

FIGURE 1. Experimental set up for the preparation of gold and iron silicide nanodomains on silicon (111).

cally friendly semiconductor and has large absorption coefficient. The optical absorption coefficient is greater than 1×10^5 cm^{-1} at 1 eV, which is 50 times larger than that of crystalline silicon (15, 16).

Interestingly, iron silicide has many phases and only the beta silicide is a semiconductor. The bulk phase diagram (see supporting information figure S5) of iron and silicon shows at least five known iron silicide compounds (Fe_3Si, Fe_5Si_3, FeSi, β-$FeSi_2$, and α-$FeSi_2$) (17). According to the phase diagram, FeSi, β-$FeSi_2$, and Fe_3Si are stable at room temperature, whereas Fe_2Si, and Fe_5Si_3 are the metastable. β-$FeSi_2$ can be fabricated by using different methods, including powder metallurgical methods (18−20), polycrystalline thin film by electron beam evaporation (21−23), magnetron sputtering (24), plasma ion processing (25), continuous wave laser and pulse laser deposition (26−28), solid phase epitaxy (29−31), reactive deposition epitaxy, molecular beam epitaxy (32, 33), and chemical vapor deposition (34).

To address some of the challenges with the outlined goals, this study investigates the reaction of colloidal iron−gold core−shell and iron−gold alloy nanoparticles with Si (111). The change in height of the heated nanoparticles is monitored by AFM to investigate how the three different nanoparticles react and collapse on the Si (111) surface. In addition, the nucleation of silicide on the deposited nanoparticles is explored, which shows catalytic activity to produce nanostructures from gas phase precursors.

EXPERIMENTAL SECTION

Gold, iron−gold alloy, and iron−gold core−shell nanoparticles are deposited on 1×1 cm^2 Si (111). Prior to the deposition, the Si (111) is washed with double distilled water and sonicated in acetone for five minutes. The clean silicon wafer is etched with 40% hydrofluoric acid for 15 minutes and dried in a vacuum. The nanoparticles are deposited on the Si (111) by dipping the silicon wafers in the nanoparticle solution for five minutes. Gold and iron−gold core−shell nanoparticles solutions are prepared in toluene and an iron−gold alloy nanoparticles solution is prepared in aqueous phase (0.01 gm nanoparticles are dissolved in 50 mL of toluene and ultrapure water in each case). After loading, the Si (111) wafer is held under vacuum ($\sim 1 \times 10^{-7}$ Torr) and heated to 500 °C at the rate of 10 °C/min. When the temperature reaches 500 °C, the wafer is maintained for 20 min in order to melt the nanoparticles on the silicon substrate. The wafers are cooled to room temperature for characterization. In the second part of the experiment, the nanoparticle-loaded wafers are annealed to 500 °C in the presence of flowing precursor molecules (triethylsilane). Argon is used as a carrier gas for the silicon precursor. The flow of argon through the silicon precursor (triethylsilane maintained at 30 °C) is controlled at constant rate of 25 mTorr during heating for 20 min. The wafers are cooled to room temperature and characterization is performed. In third part of the experiment, the nanoparticle loaded wafers are heated to 800 °C under conditions similar to that of the 2nd part of the experiment for 2 h. Experiments are carried out in the set up shown in Figure 1.

Iron−gold core−shell nanoparticles are synthesized modifying the method previously described by Wang et al. (35). Briefly, in the first step an iron seed solution is prepared and in the second step the particles are coated with gold shell. Both steps are carried out in an argon atmosphere to reduce the oxidation of the iron nanoparticles. In a typical synthesis, a solution is prepared from 0.2 mL of iron pentacarbonyl (99.9 %), 15 mL of dioctylether (99 %), 1.5 mL of oleic acid (99 %), 1.5 mL of oleyl amine (70 %), and 2.5 g of 1, 2-hexadecanediol (90 %). The solution is refluxed at 230 °C for 2.3 h. In the next step, 0.56 g of gold(III) acetate (99.9 %), 2.5 g of 1, 2-hexadecanediol, 1.5 mL of oleic acid, 2.5 mL of oleyl amine, and 25 mL of dioctylether are added to 10 mL solution of the iron nanoparticles. The solution is heated at a rate of 15 °C/min and refluxed at 210 °C for 2 h. Following this step, the solution is cooled to room temperature and treated with ethanol (99 %) to precipitate the nanoparticles. The nanoparticle slur is centrifuged at 8500 rpm for an hour and a precipitate containing the nanoparticles is deposited at the bottom of centrifuge tube. The precipitate is washed with ethanol several times and vacuum dried at room temperature for 10 h. Afterwards, the solid nanoparticles aggregates are magnetically separated from the non-magnetic part. The magnetic portion of the nanoparticles is collected and redispersed in hexane in the presence of 1.5 mL of oleic acid and 1.5 mL of oleyl amine. The experimental yield for the magnetic portion of the material is 31%.

The preparation of iron−gold alloy nanoparticles follows the previously described literature method (36). Briefly, 0.4 mL of iron pentacarbonyl (99 %) is injected into 20 mL of toluene (110 °C) containing 0.08 mol of didodecyldimethylammonium bromide. After 20 min $AuCl_3$, 3.3×10^{-4} mol,and sodium salt of mercapto propane sulphonic acid, 5.6×10^{-3} mol, are added to the solution. The gold was slowly reduced by drop wise addition of 2 mL of 2 M aqueous sodium borohydride. The nanoparticles are precipitated with ethanol and centrifuged for 15 min at 7000 rpm. The nanoparticles are washed with ethanol and chloroform several times before vacuum drying for 10 h. The magnetic part of the sample is collected for the experiments and the yield is 23%.

Detailed characterization of the etched samples is performed using tapping-mode AFM measurements. A digital instrument multimode AFM with Nanoscope IIIa electronics is employed. Tapping-mode pyramidal AFM tips are purchased from Nanosensors. Transmission electron microscopy (TEM) is performed on a Philips CM100 microscope operated at 100 kV. Powder X-ray diffraction (XRD) patterns are recorded by a Bruker D8 X-ray diffractometer with Cu Kα radiation. The scanning electron microscope (SEM, S-3500N) is used to observe the particle morphology. High-resolution transmission electron microscopy (HRTEM) is performed using a JEOL JEM2010 instrument operating at 200 kV and equipped with a LaB6 electron source.

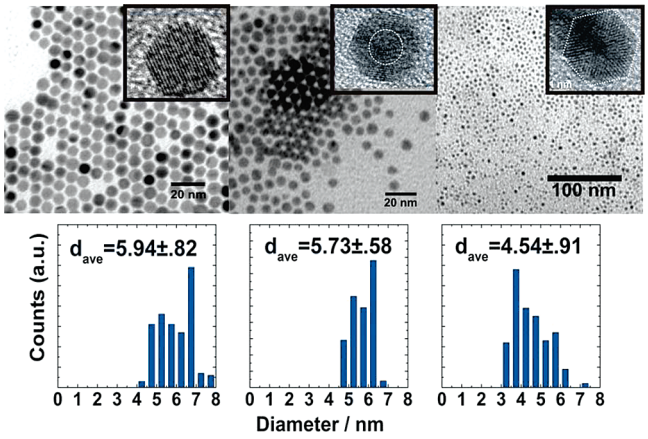

FIGURE 2. Transmission electron microscope (TEM) images of pure gold, iron–gold core–shell and iron–gold alloy nanoparticles before heating. The insets show the high-resolution transmission electron microscope (HRTEM) images of a selected nanoparticle from each sample. The histograms represent the particles distributions for each sample.

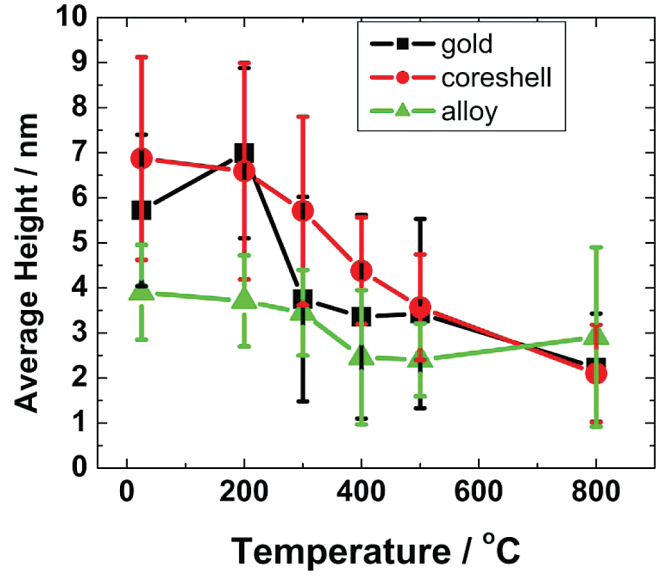

FIGURE 3. Change in height profile of iron–gold core–shell, alloy, and gold nanoparticles as a function of temperature.

X-ray photoelectron spectroscopy (XPS) analysis is performed using an Al Kα anode as the excitation source and the emitted electrons collected with a SPECS hemispherical analyzer operated at 25 eV pass energy. Any effects due to sample charging (which were minimal) were calibrated using the carbon 1s photoelectron peak (284.6 eV). Synchrotron-based X-ray absorption near edge spectroscopy (XANES) measurements were performed at the undulator beamline 8.0.1 at the Advanced Light Source, Lawrence Berkeley National Laboratory. XANES experiments were conducted using the total electron yield detection method where the total photocurrent is measured as the photon energy is scanned through the absorption edges. All spectra are normalized to the photocurrent from a gold grid. The experimental energy resolution is ~0.15 eV at the Fe L_3-edge. For both the XPS and XANES measurements, spectra are taken at base pressures of less than 5×10^{-9} Torr. Triethylsilane (97%) is used as the silicon precursor.

RESULTS AND DISCUSSION

First, the height change of the gold, iron–gold core–shell, and iron–gold alloy nanoparticles is explored during heating of the nanoparticles on the Si (111). The change in height of the nanoparticles during heating gives the approximate surface melting and diffusion behavior of the nanoparticles on the substrate. Figure 2 shows the TEM images of the gold, iron–gold core–shell, and iron–gold alloy nanoparticles used in the experiment before heating on the silicon substrate. The particles have narrow size distributions as evident by the histograms at the bottom of Figure 2. The average size distribution of these particles is determined by taking approximately 200 particles for each sample. The composition of the alloy nanoparticles and core-shell nanoparticles are 14.8 ± 4.7 mol % and 25 ± 5.0 mol % of iron, respectively. The deposition of the nanoparticles is followed by heating on the Si (111). The changes in height of the nanoparticles after heating are determined by tapping mode AFM. To increase the visibility of the particles during analysis, the AFM images of the nanoparticles on Si (111) are enhanced by taking the negative eigenvalues of the Hessian function of the images (see the Supporting Information, Figure S1). This process ensures the minimization of the artifacts associated with the AFM technique (such as spikes). The histograms of the particles are generated by the height measurement of several hundreds of the nanoparticles.

The surface roughness of the Si (111) is also measured as a reference (see the Supporting Information, Figure S2) and the root mean square (RMS) value of 0.2 nm is estimated showing very little variation when no nanoparticles are deposited on the surface. The surface treatment of the Si (111) also plays an important role in the height determination of the nanoparticles. If the surface is untreated, the nanoparticles are embedded inside the oxide layer upon heating. A similar finding has been reported by Robinson et al where they prepared a gold catalyzed silicon oxide layer on a silicon substrate (37). With substrates not treated with hydrofluoric acid, the nanoparticles submerge into the surface, therefore making the height measurements of the particles ambiguous. As an example, the impressions created by gold nanoparticles at 200 °C are shown in Figure S3b in the Supporting Information. When the surface is treated with dilute hydrofluoric acid, the native oxide layer is removed, exposing the Si (111). The same nanoparticles on the treated Si (111) do not show any impressions of oxide formation within the resolution of measurement limits (see the Supporting Information, Figure S3 left). Although the oxide layer may grow over time, its contribution to the height analysis is assumed to be negligible because the heat treatments are carried out in vacuum.

The height distributions as a function of heating temperature of the gold, iron–gold core–shell, and iron–gold alloy nanoparticles are also studied (see the Supporting Information, Figure S4). The room-temperature height distribution of the nanoparticles on Si (111) is consistent with the height distribution of the particles from the TEM image. The data show that when the particles are heated, the height distribution decreases because of the collapse of the particles. The summary of the results is shown in Figure 3 where the error bars derive from the standard deviation of the average size

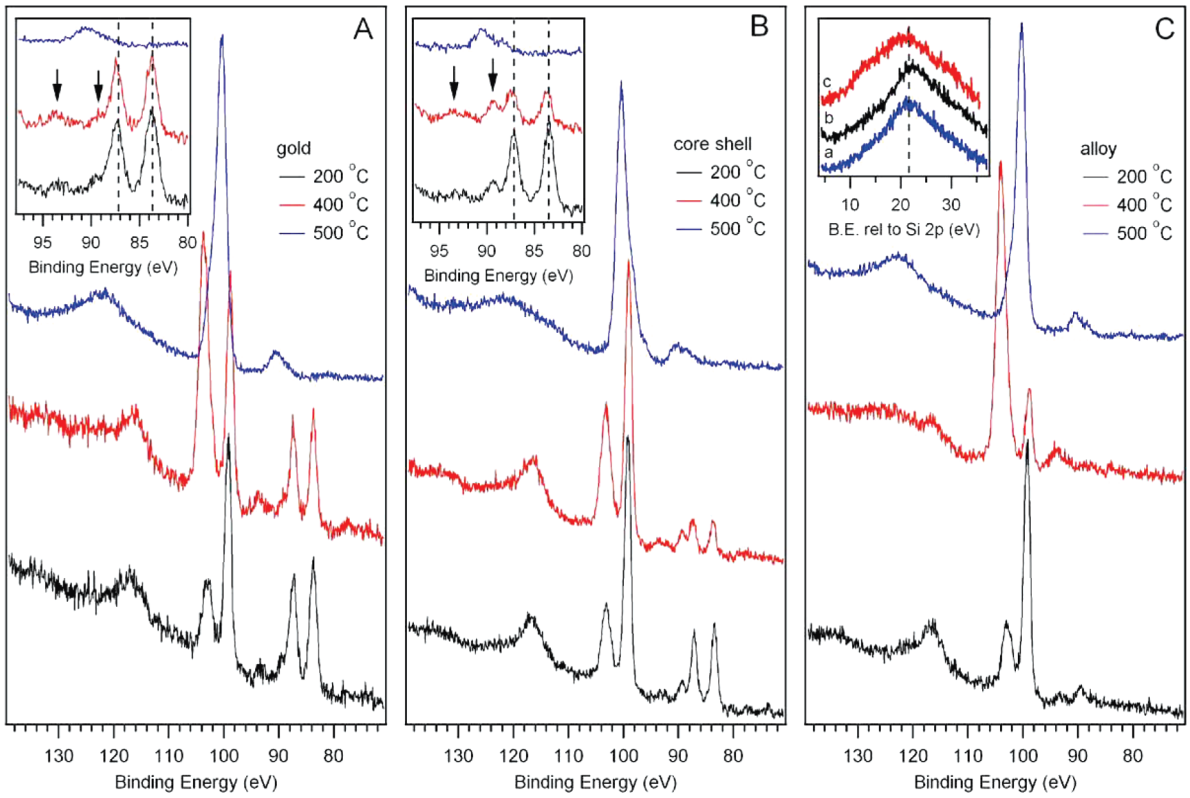

FIGURE 4. XPS spectra of (A) pure gold, (B) iron−gold core−shell, and (C) iron−gold alloy nanoparticles as a function of temperature. The insets in A and B are zoomed regions expanding the Au 4f photoelectron peaks with the traces plotted in the same order as the full scale plots. The inset in C plots the Si 2p plasmon loss feature for (a) pure gold, (b) iron−gold alloy, and (c) iron−gold core−shell nanoparticles heated at 500 °C.

and not from the error of the measurements, which is significantly smaller. First, gold nanoparticles show a slight increase in height from 25 to 200 °C. Above 300 °C, the heights of the gold nanoparticles suddenly decrease from ∼6 nm to ∼3.5 nm. The initial increase in height is most likely due to the result of coalescence followed by partial recrystallization of the nanoparticles. During coalescence and recrystallization, the clusters undergo a spontaneous shape deformation to lower their surface free energy. The height decrease above 300 °C may be the result of the gold silicide formation, which has been confirmed previously in the literature (38−43). X-ray photoelectron spectroscopy (XPS) is performed to identify the nature of the species formed during heating. As observed in Figure 4a, distinct spectral changes are observed when monitoring the Si 2p and Au 4f photoelectron peaks. At 200 °C, evidence for metallic Au ($4f_{7/2}$ photoelectron at 84 eV) and silicon (2p photoelectron at 99 eV) with a small contribution from SiO_2 (103 eV) is seen. The difference between the Si and SiO_2 peaks (3.8 eV) is consistent with previous literature (44). Interestingly, the Si(KLL) Auger peak at ∼93 eV has a noticeable shoulder at 89 eV, which has been previously reported to be a sign of alloying in silicon (45). This observation suggests that even at this lower temperature, some form of alloying is already occurring in these materials.

As the temperature is increased from 200 to 400 °C (middle trace, Figure 4a), a small shift in the Au 4f photoelectron peaks is observed, indicative of silicide formation (46). A small shift to lower binding energy for the Si 2p peaks is observed, along with a large peak at ∼104 eV. It should be noted that the origin of this peak cannot be simply ascribed to an increase in SiO_2 content for two reasons: (1) the heating steps were performed in a vacuum; therefore there is little oxygen during the process and (2) the splitting between the two peaks is now 4.9 eV, nearly 1 eV higher than the 200 °C trace. Indeed, this behavior is most likely related to the formation of the gold silicide. As the sample is further heated to 500 °C, a drastic change in the photoemission spectrum is observed (top trace, Figure 4a). First, a peak related to silicide formation is observed at ∼100.3 eV which is similar to energy shifts seen in other silicide (47, 48). Second, the metallic Au 4f photopeaks are missing; instead, they are replaced with a new gold silicide photopeak appearing at ∼90 eV. This assignment is not inconsistent with previous literature reports of large binding energy shifts in the Au 4f peaks as a function of gold oxidation state (49). The broadness of the peak at 90 eV (∼3.5 eV) versus the metallic Au peak at 84 eV (∼1.2 eV) suggests this peak is actually a broadened two component peak (comprising of both the $4f_{7/2}/4f_{5/2}$).

Core−shell nanoparticles display significantly different behavior compared to the gold nanoparticles. The overall trend still shows a decrease in the average height of the particles, but there is no sudden temperature-dependent collapse of the particles. In this case the iron core clearly plays a significant role in retarding the complete collapse of the nanoparticles, which is expected because of the higher melting point of iron. Qualitatively, the results from alloy

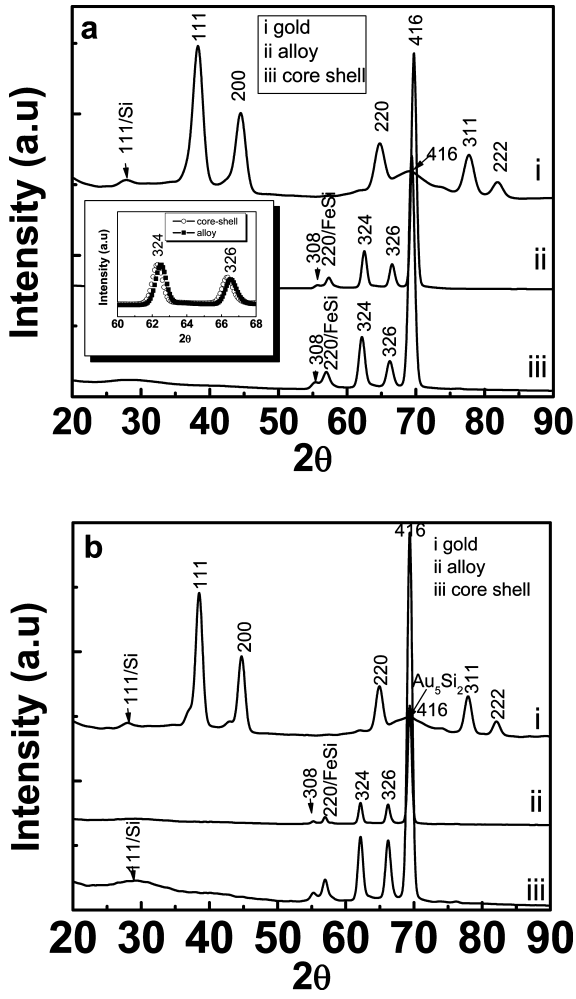

FIGURE 5. (a) XRD of (i) pure gold, (ii) iron−gold core−shell, and (iii) iron−gold alloy nanoparticles heated at 500 °C. (b) XRD of same particles after being stored for 6 months in air. The inset in the middle shows the shift in 2θ angle of alloy nanoparticles as compared with core−shell nanoparticles.

nanoparticles are similar to the results from the heating of the core−shell nanoparticles. The nanoparticles heights collapse between 300−400 °C, which is higher than that of the gold nanoparticles by approximately 100 °C. It is speculated that the difference in melting dynamics of the iron containing nanoparticles compared to the pure gold nanoparticles will lead to more efficient tethering of the particle on the surface (decreased nanoparticle mobility on the surface) via silicide formation. This suggestion is supported by the XRD results shown in Figure 5a (ii & iii). Gold silicides are less stable than the iron silicide above the eutectic temperature (363 °C) and form mostly the metastable silicides Au_3Si, Au_2Si, Au_5Si_2, and Au_7Si_5 (43, 50−52).

Figure 5a shows the XRD patterns of gold, alloy, and core−shell nanoparticles on Si (111) substrate after heating at 500 °C. The figure indicates that the gold nanoparticles remains as fcc gold with only a little amount of Au_5Si_2 formation as indicated by a small peak at 69.5° 2θ corresponding to (416) atomic reflection of fcc Au_5Si_2 (Figure 5a i). The small XRD peak at 2θ 28.4° corresponds to Si (111). The XRD peaks at 38.2, 44.4, 64.8, 77.6, and 82.0° 2θ angles correspond to the (111), (200), (220), (311), and (222) fcc atomic reflections of gold, respectively. The observation of a large amount of fcc gold via XRD is surprising from our XPS results in Figure 4A; however, when one considers the differences in depth probing between XPS and XRD, this result is not too surprising. The inelastic mean free path (IMFP), λ, of a gold 4f electron excited at 1486 eV (Al Kα) is ∼2 nm (53). The intensity, I, of the XPS experiment can be expressed as $I \propto \exp(-\lambda)$, which means that ∼95% of the signal arises from a depth of ∼3λ, indicating the probe depth of the XPS experiment is ∼6 nm. This suggests that the surface layer of these materials is comprised of the silicide, while the metallic fcc gold resides >6 nm below the surface and will be the subject of a future manuscript.

Conversely, alloy and core−shell nanoparticles form a mixture of both crystalline gold silicide Au_5Si_2 and iron mono silicide FeSi (Figure 5a ii & iii). When compared to literature values (51−59) the XRD peak at 2θ 57.0° is associated with (220) atomic reflection of iron mono silicide. General inspection of XPS spectra b and c in Figure 4 show qualitatively similar behavior to the pure gold nanoparticles. Namely, as the temperature is increased, shifting of the Si 2p photoelectron peaks is observed followed by a complete transformation of the 2p feature at 500 °C. Slight differences in line shapes may suggest different forms of silicide (i.e. both iron and gold) but analysis of the Si 2p features alone cannot provide a complete picture of iron silicide formation. It is extremely interesting to note that at 200 °C, the alloy nanoparticles show no evidence for metallic gold peaks, and the 4f photopeaks that we previously attributed to gold silicide formation do so only at higher temperatures.

Creation of iron silicide is confirmed with near-edge X-ray absorption spectroscopy (XANES) as observed in Figure 6. For both the core−shell and alloy nanoparticles, as the temperature is increased, an increase in the Fe L_3-edge XANES feature at ∼706 eV suggests formation of iron silicide (54). The formation of iron silicide is also supported from analysis of the Si plasmon features from XPS (inset, Figure 4C) where it has been reported the energy of this loss feature is a fingerprint for silicide formation (55, 56). Although we observe a plasmon energy of 17.4 eV for bulk Si (spectra not shown), the loss features for all the 500 °C treated materials fall between 21−22 eV, consistent with silicide formation.

The XRD peaks at 2θ angles 55.4, 62.2, 66.3, and 69.5° are associated with gold silicide (Au_5Si_2) (308), (324), (326), and (416) atomic reflections, respectively. Nearly identical XRD peaks of the gold silicide are observed in case of core−shell and alloy nanoparticles annealed at 500 °C in the absence of silicon precursor (Figure 5a ii & iii). However, the (416) atomic reflection is at the same 2θ in all three experiments and confirms the formation of gold silicide Au_5Si_2, but its formation is significantly higher in the cases of alloy and core−shell nanoparticles because of a catalytic effect from the iron atom. The results refer to common bimetallic catalysts where both components are present on the surface (57). Specifically, the results imply that the more oxophilic iron atom catalyzes the silicide formation attached to the neighboring, less oxophilic gold center. Furthermore,

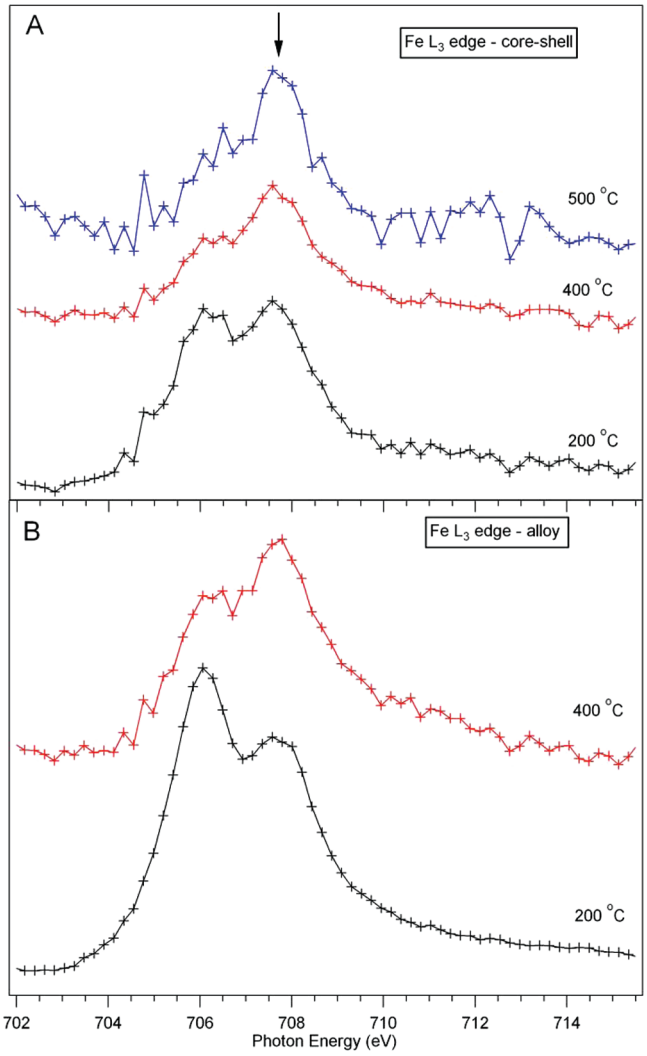

FIGURE 6. Fe L_3-edge XANES spectra for (A) iron−gold core−shell and (B) iron−gold alloy nanoparticles as a function of temperature.

iron, which has higher surface energy than gold and silicon, helps in the formation of gold silicide from core−shell and alloy nanoparticles. At room temperature, the surface free energies of thin films of iron, gold, and silicon are 2.9, 1.9, and 1.4 J m^{-2}, respectively (58−60). It is observed that both gold and iron mono silicides obtained from the alloy nanoparticles show an upward shift in XRD peak position (∼0.4°) for each peak compared to the gold and iron silicide from core-shell nanoparticles. In Figure 5a only the peak position (416) can be seen as upward shifted. The figure with overlapping scale (inset) clearly shows the shift for all reflections of silicide from alloy nanoparticles. In the core−shell nanoparticles, the active iron atoms remain protected by the gold shell (see the Supporting Information, S6) and this reduction of available iron atoms on the surface causes the significant decrease in surface potential energy and results in the observation of a lack of upward shift of XRD peak position. The average lattice constant of face centered cubic (fcc) Au_5Si_2 and iron mono silicide obtain from the alloy nanoparticles are found to be 19.49 and 4.44 Å, respectively. The values of the lattice constants obtained in this experiment are contracted compared to the reported literature values of 19.50 and 4.46 Å (52). As shown in Figure 5a ii & iii, gold silicide (Au_5Si_2) is the major crystalline (the sharp XRD peaks) product while heating the alloy and core−shell nanoparticles on the silicon substrate. The results provide an indirect piece of evidence that there is not homogeneous distribution of gold and iron silicide in the nanoparticles. The major cause of the growth of such structures is due to the relaxation of strain, which is associated with large lattice mismatch. However, thermal heating and surface reconstructions at higher temperature alter the atomic arrangements at the surface leading to change the surface potential; this might cause the formation of gold and iron silicide structures on the silicon substrate. The presence of Au_5Si_2 reported herein is different from the literature (38, 39, 41, 52, 61), where it is noted that gold can form silicide at room temperature.

Figure 5b shows the XRD patterns obtained from the same sample presented in Figure 5a after several months of exposure to air. Identical XRD spectra of the products of gold and iron−gold core−shell nanoparticles imply that there is no change in compositions of the products, i.e., there is no oxidations of the products (Figure 5b i & ii). However, the composition of alloy nanoparticles is changed and the XRD peak position of iron−gold alloy nanoparticles are shifted by ∼0.4° and overlap with the XRD peaks of silicide obtained from core−shell nanoparticles (Figure 5 iii). Neither the oxidation of iron nor the silicon is observed from the XRD results within the accuracy of the measurements. However, in case of alloy nanoparticles the more oxophilic iron atom is mostly on the surface of the nanoparticles. The oxophilic metal center may activate the silicon leading to the formation of a thin sublayer of silicon oxide or iron oxide on top of the product crystals over the time. The thin sublayer produces different residual strain on the nanoparticles surface and causes a change in the 2θ angles in the XRD spectrum.

We next investigate the effect of the presence of a silicon precursor on these nanoparticles. The sample is annealed at 500 °C (Figure 7a i) in presence of flowing triethylsilane. Upon annealing, the gold nanoparticles are completely converted into crystalline gold silicide, Au_5Si_2. Unlike in the previous case (Figure 5a i), the XRD peaks are observed at 2θ angles 62.2, 66.3, and 69.5° corresponding to (324), (326), and (416) atomic reflections of gold silicide (Au_5Si_2), respectively. Gold silicide may be formed as a result of a reaction between the gold nanoparticles and silicon from the precursor. In this experiment, silicon is supplied from substrate as well as from the gaseous precursor and ensures enough nucleation of silicon on the nanoparticles forming gold silicide. Figure 7a (ii) shows the XRD pattern obtained after annealing the sample at higher temperature (800 °C). Here only the (326) and (416) atomic reflections of gold silicide are observed, and (324) atomic reflection is absent. This process is explained based on the established literature of gold−silicon chemistry: Gold and silicon have a relatively low eutectic temperature; at higher temperature, the iron−gold mixture remains as a liquid eutectic alloy. It is reasonable to expect

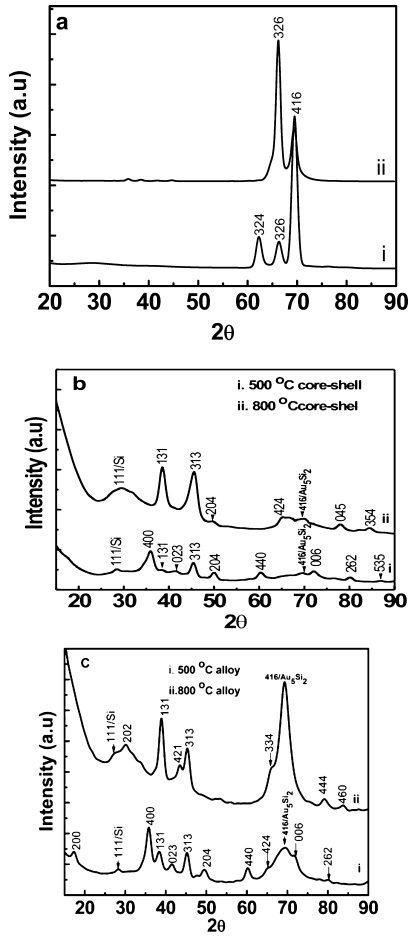

FIGURE 7. (a–c) XRD of pure gold, iron–gold core–shell, and iron–gold alloy nanoparticles heated at (i) 500 and (ii) 800 °C in the presence of flowing silicon precursor molecules.

surface crystallization and layering while cooling the samples. Subsequent solidification gives rise to non-epitaxial growth of gold silicide on top of silicon substrate. The result is composed of numerous protruding gold silicide particles with random orientation on silicon substrate as shown in Figure 8f. The atomic rearrangement due to surface dangling bond and nucleation of silicon in the nanoparticles might be expected to change atomic packing and bonding during heating. To verify the orientation of the nanostructure on silicon substrate, XRD are taken by sample rotation around the surface normal axis and no noticeable changes in the XRD data are observed, indicating that the diffracting layers consist of randomly oriented crystallites that causes the appearance and disappearance of diffraction peaks.

Figure 7b (i) shows the XRD pattern of core-shell nanoparticles annealed at 500 °C in the presence of flowing triethylsilane on silicon substrate. The figure shows that the sample forms the β-$FeSi_2$ phase on the surface after annealing. No crystalline materials are formed on the surface in the absence of the nanoparticles. The atomic reflections associated with β-$FeSi_2$ are labeled in the figure. The orthorhombic crystal structure with space group Cmca and lattice constants $a = 9.863$, $b = 7.791$, and $c = 7.833$ Å is expected to show at least 134 reflections in the XRD. However, only 11–12 XRD reflections of β-$FeSi_2$ are observed on silicon (111) substrate (either from core-shell or alloy nanoparticles). To the best of our knowledge, no complete experimental XRD spectrum of β-$FeSi_2$ nanoparticles has been presented in the literature (26, 62–70). When the sample is annealed at 800 °C with triethylsilane, the (023), (440), (006), (262), and (535) atomic reflections disappear (Figure 7b ii). New atomic reflections appear at 65.0, 78.0, and 84.4° 2θ angles corresponding to (424), (045), and (354) atomic reflections of the β-$FeSi_2$. The broadening of the (111) atomic reflection of Si is attributed to higher deposition of excess silicon from the precursor and the segregation of β-$FeSi_2$ nanoparticles due to strain-induced crystallization during annealing. Obviously, the driving force for the segregation is the difference between the surface energies of gold, iron, and silicon. Not surprisingly, at higher temperature dissociation of iron–gold pair takes place and the iron precipitates out from the active lattice sites. This is because the activation energy of diffusion for iron (0.42 eV) is lower than the activation energy of precipitation (0.7–0.9 eV) of iron at higher temperature in silicon (111) (71). The precipitated iron combines with the silicon precursor and forms the β-$FeSi_2$ as shown in images b and d in Figure 8 where the crystal size is significantly increased.

Figure 7c (i) shows the XRD pattern obtained by heating the alloy nanoparticle loaded silicon wafer in the presence of triethylsilane. The figure shows a trend similar to that of the β-$FeSi_2$ layer obtained from core-shell nanoparticles. However, the intensity of the peaks is higher and a significant broadening of the (416) peak of Au_5Si_2 is observed. The reasons for the broadening are (1) more gold atoms are exposed to the surface in the alloy; (2) a thicker layer of β-$FeSi_2$ is present, and (3) there is a high degree of segregation of atoms. Because of the segregation of atoms in the surface, a new broad (200) atomic reflection at 17.6° 2θ is observed. When the sample is annealed at 800 °C, additional reflections are observed: (202), (421), (334), (444), and (460). The presence of additional reflections implies that at higher temperature the interfacial reactions increase because of defects and surface twins that cause the change in texture of the particles, like the previous case of gold silicide. As the annealing temperature increases, the volume fraction of the nanodomains and silicon content increase indicating the growth of β-$FeSi_2$ nanostructure as shown in images b and d in Figure 8 and Table 1. The lattice mismatch between silicon substrate and the β-$FeSi_2$ layer produces the local variation of the interatomic distances in the sample and generates different XRD spectra. The crystal structure of β-$FeSi_2$ prepared from both alloy and core–shell nanoparticles are identical; only the orientation distribution is different. This difference manifests itself in the relative intensities of the diffraction peaks. Similar to the β-$FeSi_2$ obtained from core–shell nanoparticles, no XRD peak for either gold or gold silicide is observed in the case of alloy nanoparticles. It is important to note that the Si (111) atomic reflections are not observed either in the case of alloy nanoparticles heated in absence of precursor (Figure 5a, ii and 5b,ii) or

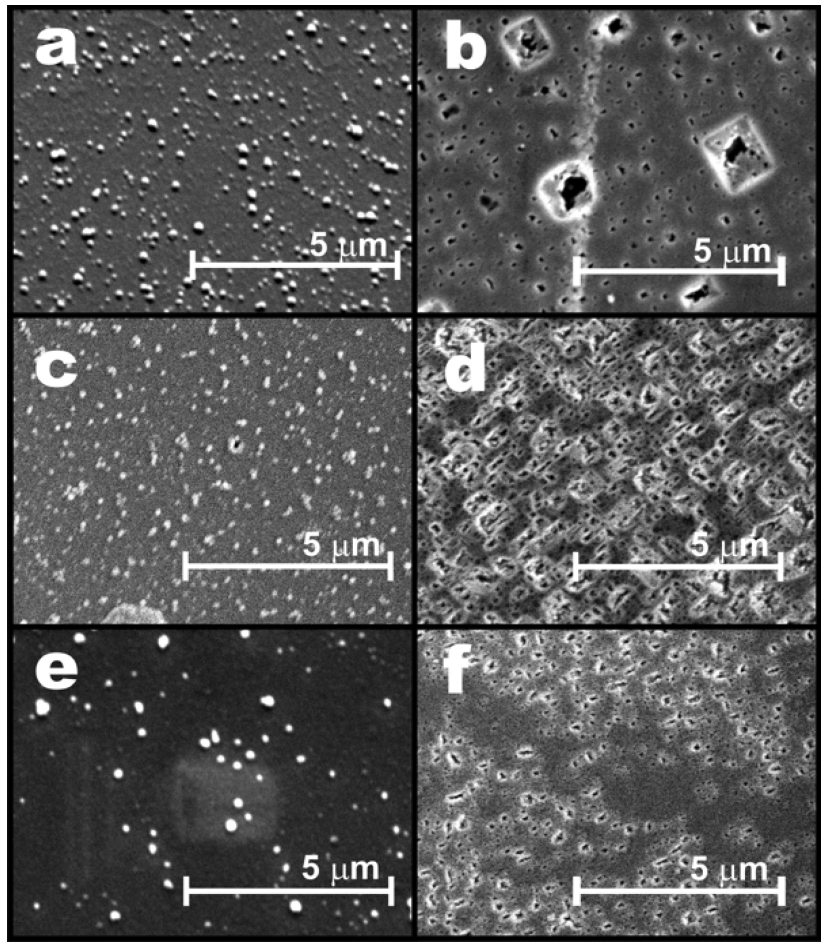

FIGURE 8. (a, b) SEM images of iron−gold core−shell nanoparticles heated at 500 and 800 °C in the presence of flowing precursor molecules, respectively. (c, d) SEM images of iron−gold alloy nanoparticles heated at 500 and 800 °C in the presence of flowing precursor molecules, respectively, and (e, f) SEM images of gold nanoparticles heated at 500 and 800 °C in the presence of flowing precursor molecules.

Table 1. Composition of Iron Silicide from EDX Measurements at Two Different Temperatures; Obtained from Gold−Iron Core−Shell and Alloy Nanoparticles

	iron silicide from Fe−Au alloy				iron silicide from Fe−Au core−shell				silicon wafer + silicon precursor		silicon wafer only	
	500 °C		800 °C		500 °C		800 °C		500 °C		500 °C	
element	wt %	at %	wt %	at %	wt %	at %	wt %	at %	wt %	at %	wt %	at %
silicon K	46.72	32.77	54.94	42.85	40.65	26.33	46.63	31.63	25.86	100.00	0.35	100.00
iron K	8.33	7.83	8.22	9.17	16.60	12.64	16.35	9.64				
gold M	4.37	0.41	3.62	0.38	3.81	0.38						
carbon K	35.33	54.47	30.77	44.19	35.47	56.50	37.02	58.73				
oxygen K	1.87	2.16	2.45	3.41	3.47	4.15						
sulphur K	1.61	0.93										
sodium K	1.77	1.43										

for gold nanoparticles heated in the presence of triethylsilane (Figure 7a, i & ii).

In images a and b in Figure 8, the scanning electron microscope (SEM) images of iron−gold core-shell nanoparticles deposited on Si (111) and heated in the presence of triethylsilane at 500 °C and 800 °C are shown. The morphology of the particles at 500 °C is not significantly different from that of the particles deposited at room temperature (data not shown). When the sample is annealed at 800 °C, the image shows dramatic changes in the morphology and in the contrast of the particles. The particles appear more crystalline and they show some order on the surface. A similar phenomenon is observed in case of iron−gold alloy nanoparticles at 800 °C as shown in images c and d in Figure 8. The results are consistent with the XRD results shown previously, where fewer atomic reflections are observed at 800 °C because of the preferred orientation of the particles on the silicon substrate. In the case of gold nanoparticles, the preferred orientation is not observed as shown in images e and f in Figure 8. The partial ordering observed in images b and d in Figure 8 is probably the result of the single-crystal substrate. When the iron containing part of the catalyst

forms the iron silicide, cracks develop, which leads to some migration of the other nanoparticles into the crack, leading to the observed pattern (67, 72).

Compositions of the silicides that are obtained after heating the alloy and core−shell nanoparticles in presence of triethylsilane are listed in Table 1. The composition is measured by using energy-dispersive X-ray analysis (EDX) attached to the SEM. The comparison of the surface composition of the iron silicide obtained from core−shell nanoparticles at 500 and 800 °C shows that the silicon concentration is increasing, but the relative amount of iron remains almost the same. As expected, silicon is nucleating in the nanoparticles and forms the β-$FeSi_2$ nanoparticle layer. At 800 °C, interestingly, gold is not observed, probably because of gold silicide instability and iron precipitate out forming iron silicides. In the case of the iron−gold alloy nanoparticles, the amount of silicon at 800 °C also increases compared to the sample heated to 500 °C. The relative amount of gold is reduced, similar to the results using core−shell nanoparticles. At the same time, sodium and sulfur are completely removed, and the amount of oxygen is increased from desorption of ligands (sodium salt of mercapto-3 propane sulphonic acid). The absence of sodium, sulfur, and the reduced amount of carbon at 800 °C shows removal of ligands from the nanoparticles.

CONCLUSIONS

This work has explored the possibilities of using composite iron−gold, core−shell, alloy, and gold nanoparticles to form iron and gold silicide (β-$FeSi_2$, FeSi, Au_5Si_2). Heating the composite nanoparticles at different temperatures reveals distinctly different behaviors. Gold collapses at lower temperature because of the formation of gold silicide. The formation of gold silicide is catalyzed by iron atom. The iron-containing nanoparticles collapse at a significantly higher temperature. The silicide is also formed from the gas phase silicon precursor of triethylsilane, which means that the nanoparticles are available for nucleation. The β-$FeSi_2$ obtained in this experiment is a narrow band gap semiconductor and potential photovoltaic material. Although the iron silicide system has not currently been the subject of much attention in the literature, simple strategies for the preparation of these materials, like those presented in this manuscript, could prove to be of great potential and very useful for future studies on nanostructured iron silicides.

Acknowledgment. The authors are grateful to the Department of Chemistry at Kansas State University for funding. The Advanced Light Source is supported by the Director, Office of Science, Office of Basic Energy Sciences, U.S. Department of Energy, under Contract DE-AC02-05CH11231.

Supporting Information Available: A method of AFM image analysis to increase the accuracy of height measurements of nanoparticles; AFM images of the nanoparticles on etched and unetched silicon (111) substrate and AFM image of Si (111) without the nanoparticles; histograms of the height measurements of the nanoparticles at six different temperatures; phase diagram of iron−silicon system; and XRD of iron−gold core−shell nanoparticles at 25 and 500 °C (PDF). This material is available free of charge via the Internet at http://pubs.acs.org.

REFERENCES AND NOTES

(1) Selim, S. *Angew. Chem. Int. Ed.* **2001**, *40* (2), 312–329.
(2) Kim, B. J.; Tersoff, J.; Kodambaka, S.; Reuter, M. C.; Stach, E. A.; Ross, F. M. *Science* **2008**, *322* (5904), 1070–1073.
(3) Wang, W.; Lu, X. L.; Zhang, T.; Zhang, G. Q.; Jiang, W. J.; Li, X. G. *J. Am. Chem. Soc.* **2007**, *129* (21), 6702+.
(4) Wang, H. T.; Xie, Z. P.; Yang, W. Y.; Fang, J. Y.; An, L. N. *Crystal Growth Des.* **2008**, *8* (11), 3893–3896.
(5) Nagashima, K.; Yanagida, T.; Oka, K.; Tanaka, H.; Kawai, T. *Appl. Phys. Lett.* **2008**, *93* (15).
(6) Dick, K. A.; Deppert, K.; Karlsson, L. S.; Wallenberg, L. R.; Samuelson, L.; Seifert, W. *Adv. Fun. Mater.* **2005**, *15* (10), 1603–1610.
(7) Dai, Z. R.; Pan, Z. W.; Wang, Z. L. *Adv. Funct. Mater.* **2003**, *13* (1), 9–24.
(8) Kamat, P. V. *J. Phys. Chem. C* **2007**, *111* (7), 2834–2860.
(9) Buonassisi, T.; Istratov, A. A.; Marcus, M. A.; Lai, B.; Cai, Z. H.; Heald, S. M.; Weber, E. R. *Nat. Mater.* **2005**, *4* (9), 676–679.
(10) Brown, P.; Kamat, P. V. *J. Am. Chem. Soc.* **2008**, *130* (28), 8890+.
(11) Farrow, B.; Kamat, P. V. *J. Am. Chem. Soc.* **2009**, *131* (31), 11124–11131.
(12) Jose, R.; Thavasi, V.; Ramakrishna, S. *J. Am. Ceram. Soc.* **2009**, *92* (2), 289–301.
(13) Christensen, N. E. *Phys. Rev. B* **1990**, *42* (11), 7148.
(14) Antonov, V. N.; Jepsen, O.; Henrion, W.; Rebien, M.; Stauss, P.; Lange, H. *Phys. Rev. B* **1998**, *57* (15), 8934–8938.
(15) Liu, Z. X.; Osamura, M.; Ootsuka, T.; Kuroda, R.; Makita, Y.; Tanoue, H.; Fukuzawa, Y.; Otogawa, N.; Nakayama, Y. *Thin Solid Films* **2006**, *515* (4), 1532–1538.
(16) Matsumoto, M.; Sugie, K.; Kawauchi, T.; Fukutani, K.; Okano, T. *Jpn. J. Appl. Phys.* **2006**, *45* (3B), 2390–2394.
(17) Hansen, M.; Anderko, K. *Constitution of Binary Alloys*, second ed.; McGraw-Hill Book Company: New York, 1958; p 713.
(18) Gross, E.; Riffel, M.; Stohrer, U. *J. Mater. Res.* **1995**, *10* (1), 34–40.
(19) Birkholz, U.; Finkenra., H; Naegele, J.; Uhle, N. *Phys. Status Solidi* **1968**, *30* (1), K81.
(20) Kojima, T. *Phys. Status Solidi A* **1989**, *111* (1), 233–242.
(21) Herz, K.; Powalla, M. *Appl. Surf. Sci.* **1995**, *91* (1−4), 87–92.
(22) Won, J.; Kovacs, A.; Naito, M.; Ishimaru, M.; Hirotsu, Y., *J. Appl. Phys.* **2007**, *102* (10).
(23) Takakura, K.; Ohyama, H.; Takarabe, K.; Suemasu, T.; Hasegawa, F., *J. Appl. Phys.* **2005**, *97* (9).
(24) Komabayashi, M.; Hijikata, K.; Ido, S. *Jpn. J. Appl. Phys.* **1991**, *30* (2), 331–334.
(25) Heinrich, A.; Griessmann, H.; Behr, G.; Ivanenko, K.; Schumann, J.; Vinzelberg, H. *Thin Solid Films* **2001**, *381* (2), 287–295.
(26) Yoshitake, T.; Nakagauchi, D.; Nagayama, K. *Jpn. J. Appl. Phys.* **2003**, *42* (7B), L849–L851.
(27) Yoshitake, T.; Nagamoto, T.; Nagayama, K. *Thin Solid Films* **2001**, *381* (2), 236–243.
(28) Yoshitake, T.; Nagamoto, T.; Nagayama, K. *Mater. Sci. Eng., B* **2000**, *72* (2−3), 124–127.
(29) Lefki, K.; Muret, P.; Cherief, N.; Cinti, R. C. *J. Appl. Phys.* **1991**, *69* (1), 352–357.
(30) Gallego, J. M.; Miranda, R. *J. Appl. Phys.* **1991**, *69* (3), 1377–1383.
(31) Kataoka, K.; Hattori, K.; Miyatake, Y.; Daimon, H. *Phys. Rev. B* **2006**, *74* (15).
(32) Yoshiaki, N.; Yasushi, N.; Sung-Pyo, C.; Nobuo, T.; Masakazu, I. *J. Appl. Phys.* **2006**, *100* (4), 044313.
(33) Peale, D. R.; Haight, R.; Ott, J. *Appl. Phys. Lett.* **1993**, *62* (12), 1402–1404.
(34) Zybill, C. E.; Huang, W. *Inorg. Chim. Acta* **1999**, *291* (1−2), 380–387.
(35) Wang, L.; Luo, J.; Maye, M. M.; Fan, Q.; Rendeng, Q.; Engelhard, M. H.; Wang, C.; Lin, Y.; Zhong, C.-J. *J. Mater. Chem.* **2005**, *15* (18), 1821–1832.
(36) Dahal, N.; Chikan, V.; Jasinski, J.; Leppert, V. J. *Chem. Mater.* **2008**, *20* (20), 6389–6395.
(37) Robinson, J. T.; Evans, P. G.; Liddle, J. A.; Dubon, O. D. *Nano Lett.* **2007**, *7* (7), 2009–2013.

(38) Baumann, F. H.; Schroter, W. *Phys. Rev. B* **1991**, *43* (8), 6510–6519.
(39) Hiraki, A.; Nicolet, M. A.; Mayer, J. W. *Appl. Phys. Lett.* **1971**, *18* (5), 178–181.
(40) Paulose, M.; Varghese, O. K.; Grimes, C. A. *J. Nanosci. Nanotechnol.* **2003**, *3* (4), 341–346.
(41) Wolffenbuttel, R. F. *Sens. Actuators, A* **1997**, *62* (1−3), 680–686.
(42) Zichichi, A. *Silicides Fundamentals and Applications*; World Scientific: Singapore, 2000.
(43) Ashtikar, M. S.; Sharma, G. L. *Jpn. J. Appl. Phys.* **1995**, *34* (10), 5520–5526.
(44) Cates, M.; Miller, D. R. *Phys. Rev. B* **1983**, *28* (6), 3615.
(45) Hiraki, A.; Kim, S. C.; Imura, T.; Iwami, M. *Jpn. J. Appl. Phys.* **1979**, *18* (9), 1767–1772.
(46) Sundaravel, B.; Sekar, K.; Kuri, G.; Satyam, P. V.; Dev, B. N.; Bera, S.; Narasimhan, S. V.; Chakraborty, P.; Caccavale, F. *Appl. Surf. Sci.* **1999**, *137* (1−4), 103–112.
(47) Prabhakaran, K.; Sumitomo, K.; Ogino, T. *Appl. Phys. Lett.* **1996**, *68* (9), 1241–1243.
(48) Brause, M.; Braun, B.; Ochs, D.; Maus-Friedrichs, W.; Kempter, V. *Surf. Sci.* **1998**, *398* (1−2), 184–194.
(49) Kishi, K.; Ikeda, S. *J. Phys. Chem.* **1974**, *78* (2), 107–112.
(50) Comrie, C. M.; Falepin, A.; Richard, O.; Bender, H.; Vantomme, A. *J. Appl. Phys.* **2004**, *95* (5), 2365–2370.
(51) Khalfaoui, R.; Benazzouz, C.; Guittoum, A.; Tabet, N.; Tobbeche, S. *Vacuum* **2006**, *81* (1), 45–48.
(52) Tsaur, B. Y.; Mayer, J. W. *Philos. Mag., A* **1981**, *43* (2), 345–361.
(53) http://www.lasurface.com/imfp.
(54) Esaka, F.; Yamamoto, H.; Matsubayashi, N.; Yamada, Y.; Sasase, M.; Yamaguchi, K.; Shamoto, S.; Magara, M.; Kimura, T. *Appl. Surf. Sci.* **2010**, *256*, 3155–3159.
(55) Miquita, D. R.; Gonzalez, J. C.; da Silva, M. I. N.; Rodrigues, W. N.; Moreira, M. V. B.; Paniago, R.; Ribeiro-Andrade, R.; Magalhaes-Paniago, R.; Pfannes, H. D.; de Oliveira, A. G. *J. Vac. Sci. Technol., A* **2008**, *26* (5), 1138–1148.
(56) Egert, B.; Panzner, G. *Phy. Rev. B* **1984**, *29* (4), 2091.
(57) Alayoglu, S.; Nilekar, A. U.; Mavrikakis, M.; Eichhorn, B. *Nat. Mater.* **2008**, *7* (4), 333–338.
(58) Pastor, C. J.; Limones, C.; Hinarejos, J. J.; Garcia, J. M.; Miranda, R.; GomezGoni, J.; Ortega, J. E.; Abruna, H. D. *Surf. Sci.* **1996**, *364* (1), L505–L510.
(59) Hara, S.; Izumi, S.; Kumagai, T.; Sakai, S. *Surf. Sci.* **2005**, *585* (1−2), 17–24.
(60) Palasantzas, G.; Vystavel, T.; Koch, S. A.; De Hosson, J. T. M *J. Appl. Phys.* **2006**, *99* (2).
(61) Green, A. K.; Bauer, E. *J. Appl. Phys.* **1976**, *47* (4), 1284–1291.
(62) Yoshitake, T.; Yatabe, M.; Itakura, M.; Kuwano, N.; Tomokiyo, Y. *Appl. Phys.Lett.* **2003**, *83* (15), 3057–3059.
(63) Wan, Q.; Wang, T. H.; Lin, C. L. *Appl. Phys. Lett.* **2003**, *82* (19), 3224–3226.
(64) Udono, H.; Kikuma, I. *Jpn. J. Appl. Phys.* **2001**, *40* (3A), 1367–1369.
(65) Pan, S. S.; Ye, C.; Teng, X. M.; Fan, H. T.; Li, G. H. *Phys. Status Solidi A* **2007**, *204* (10), 3316–3320.
(66) Muret, P.; Ali, I.; Brunel, M. *Semicond. Sci. Technol.* **1998**, *13* (10), 1170–1179.
(67) Liu, Z.; Osamura, M.; Ootsuka, T.; Kuroda, R.; Makita, Y.; Tanoue, H.; Fukuzawa, Y.; Otogawa, N.; Nakayama, Y. *Thin Solid Films* **2006**, *515* (4), 1532–1538.
(68) Kakemoto, H.; Makita, Y.; Sakuragi, S.; Tsukamoto, T. *Jpn. J. Appl. Phys.* **1999**, *38* (9A), 5192–5199.
(69) Datta, A.; Kal, S.; Basu, S.; Nayak, M.; Nath, A. K. *J. Mater. Sci.* **1999**, *10* (9), 627–631.
(70) Bayazitov, R. M.; Batalov, R. I. *J. Phys.: Condens. Matter* **2001**, *13* (5), L113–L118.
(71) Brotherton, S. D.; Bradley, P.; Gill, A. *J. Appl. Phys.* **1985**, *57* (6), 1783–1790.
(72) Liu, Z., Wang, S., Otogawa, N., Osamura, M., Ootsuka, T., Mise, T., Suzuki, Y., Fukuzawa, Y., Nakayama, Y., Tanoue, H., Makita, Y. *3rd World Conference on Photovoltaic Energy Conversion* ; Osaka, Japan, May 11−18, 2003; IEEE: Piscataway, NJ, 2003; poster 126−129.

AM100282Q